Title

Bound States in the Continuum on a Silicon Chip with Dynamic Tuning

Authors

Gong, Zilun
Serafini, John
Yang, Fuyi
et al.

Peer reviewed

Bound States in the Continuum on a Silicon Chip with Dynamic Tuning

Zilun Gong[1,2] John Serafini,[3] Fuyi Yang,[1,2] Stefan Preble,[3] and Jie Yao[1,2,*]

[1]*Department of Materials Science and Engineering, University of California Berkeley, Berkeley, California 94720, USA*

[2]*Materials Sciences Division, Lawrence Berkeley National Laboratory, Berkeley, California 94720, USA*

[3]*Microsystems Engineering, Rochester Institute of Technology, Rochester, New York 14623, USA*

Expanding bound states in the continuum (BIC) beyond photonic crystal systems may enable broader applications benefiting from the unique properties of BIC states. We use photonic integrated circuit to realize a Fabry-Pérot BIC on a silicon chip. The devices consist of cascaded ring resonators with tunable resonance frequencies and phase delays. As a result, the BIC state is dynamically tuned with electrical I/O. We analyze the mechanism of the formation of BIC states in this waveguide system and point out the fundamental differences between the BIC states and electromagnetically induced transparency states in integrated photonics. The high transmission protected by the BIC state enables versatile optical filters, which are capable of independent control over switching, peak position, and quality factor. We also demonstrate the scalability of this platform. This integrated silicon photonic platform brings opportunities for practical BIC applications.

Bound states in the continuum (BIC) are confined resonances amid a continuous spectrum of radiating channels. This phenomenon was initially proposed in quantum mechanics but was recently proven to be a much more generic behavior of all physical waves [1]. Notably, photonic crystal (PhC) slabs have become a promising platform for BIC studies [2]. Initially, the symmetry mismatch between some modes at high-symmetry points, e.g., Γ points of PhC slabs, and free space polarizations will introduce robust BIC states protected by the symmetry [3]. Recently, a fine-tuned BIC off the Γ point was proposed as a result of the perfect cancellation of outgoing waves [4]. Moreover, those BIC states are polarization singularities that carry nontrivial topological charges, which provides a different perspective in topological photonics research [5,6].

In addition to giving birth to rich physics, BIC states and near-BIC states are inherently high-quality-factor (Q-factor) resonance modes, which bring about potential applications such as enhancement of nonlinear phenomena [7] and lasing [8,9]. In addition, one can merge multiple BIC states using a PhC slab so that the near-BIC states can acquire even higher Q. Therefore, even deviations from the exact BIC state due to fabrication errors are unlikely to compromise the Q-factor [10]. Also, the nature of the polarization singularity at BIC

states promises a lasing source with a polarization vortex, which gives rise to another degree of freedom in optical communications [11,12].

To date, most photonic BIC demonstrations and applications have been realized in PhC slab systems. Although PhC slabs have their engineering flexibilities, such as those of material, lattice symmetry, and band structure, the success of BIC realizations in PhC slabs requires a large area of low-defect periodic structures and out-of-plane excitations [4,13]. In addition, symmetry-protected BICs have been demonstrated in special waveguides based on anisotropic materials. The need for strongly anisotropic materials substantially limits their applications. The realizations of BICs in silicon photonics are still lacking [14,15].

Besides the enhanced light-matter interaction in lasing applications, the high-Q nature of BICs also poses an opportunity for versatile filters, which is compatible with photonic integrated circuits (PICs) and complementary metal oxide semiconductor (CMOS) technology [16]. By definition, high-Q modes have long lifetimes and low coupling rates (coefficients) to and/or from the continuum (delocalized states). At the BIC or near-BIC point, the photon hardly "sees" the resonator system but instead passes through [4], which is useful for realizing a transparency window.

In this paper, we demonstrate the realization of BIC on a silicon chip, in particular, BIC filter devices on an active CMOS-compatible PIC platform, where the existence of

———
[*]yaojie@berkeley.edu

the transmission peak, together with the peak position and peak width (Q-factor), can all be independently and dynamically controlled. We also clarify the fundamental difference between such BIC modes and the electromagnetically induced transparency (EIT) phenomena in PICs. We believe it is a leap forward towards practical applications of BIC states, and it provides a different methodology for PIC device design.

We utilize the Fabry-Pérot (FP) BIC states in this paper [1,17]. With parameter tuning, we can make one output channel and the resonant radiation interfere and cancel each other. Figure 1(a) shows a schematic structure of its realization: the two cascaded resonators have their intrinsic resonance frequencies ω_1 and ω_2, respectively. The two resonators do not crosstalk directly; instead they only couple through the bus waveguides. If we assume the coupling rates at all gaps are $\gamma_c/2$, and the intrinsic loss rate $\gamma_i/2$ is negligible, the Hamiltonian of the resonator system is

$$ H = \begin{pmatrix} \omega_o + \Delta & 0 \\ 0 & \omega_o - \Delta \end{pmatrix} - i\frac{\gamma_c}{2} \begin{pmatrix} 1 & e^{i\Delta\varphi} \\ e^{i\Delta\varphi} & 1 \end{pmatrix}, \quad (1) $$

where $\omega_o = (\omega_1 + \omega_2)/2$ is the center frequency, $\Delta = (\omega_1 - \omega_2)/2$ is the resonance detuning, and $\Delta\varphi$ is the phase shift between the two resonators. Then we can further simplify the model by assuming that $\Delta\varphi$ is an integer multiple of π, i.e., $\Delta\varphi = m\pi$, so that the round trip satisfies the FP resonance condition (we call it "system on-resonance"). The eigenvalue of the resonator system is therefore

$$ \omega_\pm = \omega_o - i\frac{\gamma_c}{2} \pm \sqrt{\Delta^2 - \frac{\gamma_c^2}{4}}. \quad (2) $$

If there is no resonance detuning, i.e., $\Delta = 0$, ω_o is the real eigenvalue of the system. This means that the lifetime of this mode is infinitely long, and this is a FP BIC state [1].

However, if we allow a small frequency detuning compared to the coupling rate ($\gamma_c/2 \gg \Delta$), we can still write the eigenvalue using a first-order Taylor expansion:

$$ \omega_\pm \approx \omega_o - i\frac{\gamma_c}{2} \pm i\frac{\gamma_c}{2}\left(1 - \frac{4\Delta^2}{\gamma_c^2}\right). \quad (3) $$

Then $\omega_o - 2i\Delta^2/\gamma_c$ is one of the eigenvalues, while ω_o is a near-BIC state of the resonator system.

We then derive the transmission characteristics for the resonator system using temporal-coupled-mode theory [17–19] (Appendix A).

If the probe frequency is ω_o, the transmission is protected by near-BIC state with $T \to 1$:

$$ t_{\mathrm{BIC}} = \frac{\Delta^2 + (\gamma_i^2/4)}{\Delta^2 + \gamma_c\gamma_i + (\gamma_i^2/4)} \approx \frac{\Delta^2}{\Delta^2 + \gamma_c\gamma_i} \to 1. \quad (4) $$

On the contrary, if the probe frequency coincides with one of the intrinsic resonance frequencies of the two resonators, $T \to 0$:

$$ t_{\omega_1(\omega_2)} = \frac{\pm i\gamma_i\Delta + (\gamma_i^2/4)}{\pm i\gamma_i\Delta \pm 2i\gamma_c\Delta + \gamma_c\gamma_i + (\gamma_i^2/4)} $$
$$ \approx \frac{1}{1 + 2(\gamma_c/\gamma_i) \mp i(\gamma_c/\Delta)} \to 0. \quad (5) $$

To summarize, in a cascaded resonator system, if we fine-tune the phase delay between two resonators to make the system on-resonance, the center frequency becomes a near-BIC point. Coupling into this mode from the continuum is difficult, which gives rise to high transmission. Additionally, the transmission at ω_1 and ω_2 is low. Therefore, we can obtain an artificial transparency window that can be fully controlled by ω_1 and ω_2: ω_o determines the peak position, while Δ controls the peak width and Q-factor. In addition, we can also turn the peak off by breaking the resonance condition or diminishing resonance detuning Δ.

In addition, we would like to address the seemingly contradicting phenomena that the exact-BIC state leads to total reflection while the near-BIC state has high transmission. BIC and near-BIC states are high-Q states where coupling from the radiation continuum is difficult (energy stays in the continuum), which does not guarantee the direction of the output energy. From Eq. (4), the direction of output is a competing result between Δ and γ_i: for the exact-BIC state $\Delta = 0$, so it shows high reflection; for the near-BIC state $\Delta \gg \gamma_i$, so it shows high transmission instead.

Such transmission characteristics share some similarities with the optical analog of EIT in atomic physics. However, there are some fundamental differences between them [20–26]. Figure 1(d) is the energy-level diagram of the rigorous optical analog of EIT. A low-Q resonator couples to the ground state, while a high-Q resonator only couples to the low-Q resonator with a coupling rate J. J is the analog of the Rabi frequency in the original EIT [20]. This system can be realized using two directly coupled resonators and a single bus. EIT is a particular Fano resonance where two resonators have disparate Q-factors but the same resonance frequency. In other words, their energy levels should have zero offsets [27,28]. It is possible to construct an EIT analog with indirectly coupled resonators. However, the system still needs to follow the Fano resonance condition. We can simulate this effect by tweaking the setup following the energy-level diagram in Fig. 1(e). We lower the Q-factor of the first resonator and reduce the coupling rate of the second resonator while fixing their resonance wavelengths at 1533 nm. Here the Fano resonance results in the transparency window [Fig. 1(g)]. The shape of the peak is affected by the Q-factor difference and symmetry of the feedback loop [28]. In summary, the transparency window in a rigorous EIT analog is a result of Fano resonance (with two overlapping resonances), which is not valid for the near-BIC state.
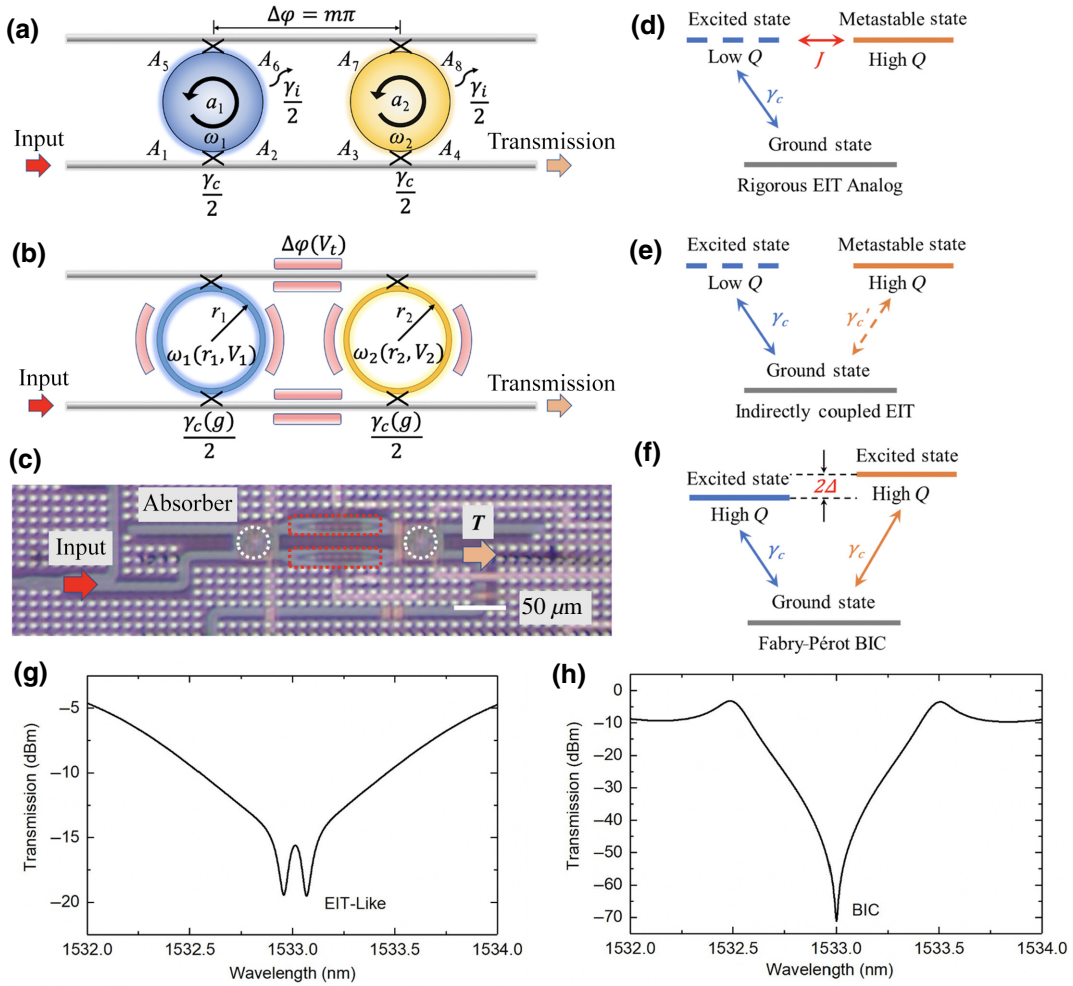
FIG. 1. (a) A schematic model of the dual-resonator system that demonstrates Fabry-Pérot BIC. A_1 to A_8 are the electric field amplitudes in the bus near the coupling ports, a_1 and a_2 are the amplitudes of the resonance modes at steady state, and ω_1 and ω_2 are the intrinsic resonance frequencies of the two resonators. The intrinsic decay rate is $\gamma_i/2$ for both resonators; the coupling rate is $\gamma_c/2$ at all the gaps. (b) Schematic of a silicon photonics realization. Two ring resonators have slightly different radii (r_1, r_2) coupling through two bus waveguides. The gaps (g) between rings and buses are of the same size to enforce the same coupling rate $\gamma_c(g)/2$. Thermo-optic heaters (pink bars) tune ω_1, ω_2, and $\Delta\varphi$ with independent control voltages (V_1, V_2, and V_t). (c) Optical image from the fabricated dual-resonator device. White circles denote the ring resonators, red rectangles are the thermo-optic phase shifters. (d)–(f) Energy-level diagrams of rigorous EIT analog, indirectly coupled EIT, and Fabry-Pérot BIC, respectively. 2Δ is the frequency offset between two resonators, J is the direct coupling rate between two resonators, and $\gamma_c(\gamma'_c)$ is the coupling rate between ground state and excited states. (g),(h) Simulation of EIT-like (Fano resonance) and BIC transmission with zero energy offset ($\Delta = 0$) between two resonators. Spectra are plotted as functions of probe beam detuning relative to resonance wavelength (1533 nm).

Figure 1(f) is the energy-level diagram of the FP BIC. The two energy levels (resonators) have similar Q-factors that couple indirectly through the continuum. The transmission window requires the energy offset Δ, distinctive from the requirements of a rigorous optical EIT. Figure 1(h) is the simulation result of the BIC state with two identical resonators ($\Delta = 0$); both have a resonance wavelength of 1533 nm. The transmission spectrum shows complete reflection at the BIC point.

Based on the derivation [Eq. (4)], we designed the filter device [Fig. 1(b)] shown in Fig. 1(c) (Appendix B), whose transmission characteristics are summarized in Fig. 2. The blue curve in Fig. 2(a) is an example of a BIC filter, which is also the reference curve in other panels. The two rings have their intrinsic resonant wavelengths at 1532.4 and 1533.4 nm, respectively. The phase delay between the two rings is tuned to make the system on-resonance. The transmission at intrinsic resonance wavelengths is low, while the center wavelength is the protected near-BIC state with high transmission. This result agrees with the model very well. If we increase the phase delay between the two rings by increasing the voltage of the phase shifter (green and
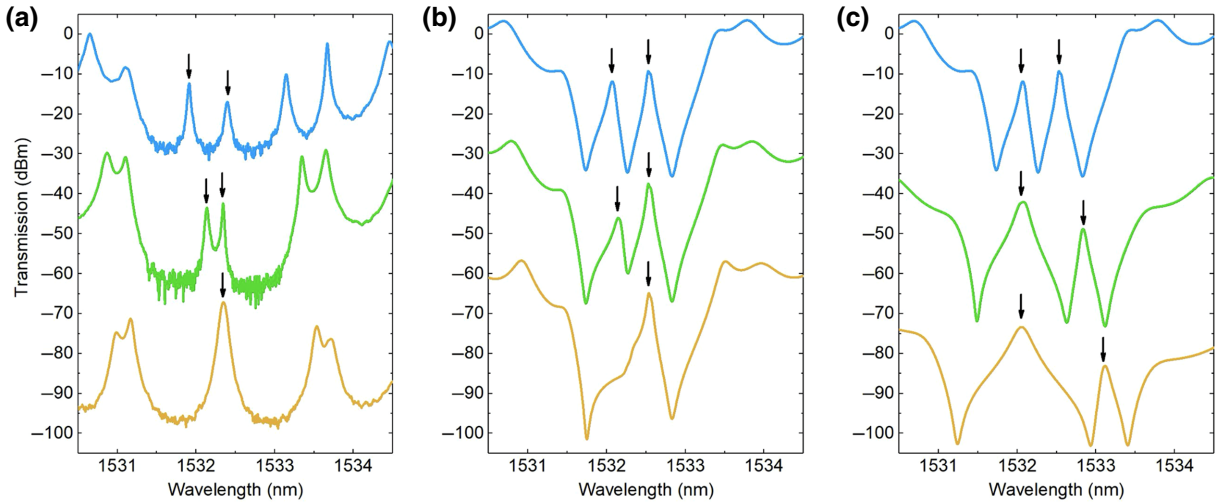
FIG. 2. Transmission spectra of BIC filters. (a) Tuning the phase delay between two rings. The first curve is the on-resonance case with a symmetric transparency window. V_t is the voltage of the phase shift heater between two rings. (b) Tuning the peak position with fixed width. (c) Tuning the peak width (Q-factor) with fixed position. Spectra in (b) and (c) are all on-resonance. Blue curves in (a)–(c) are the same. Black arrows are used as a guide to the peaks of interest in each panel. All the curves are shifted vertically for clear illustration. Black, blue, and red arrows highlight ω_o, ω_1, and ω_2, respectively, as described in Eqs. (4) and (5). Simulation counterparts can be found in Appendix B

yellow curves), the FP resonance condition is not seen. The transparency window red-shifts and the peak becomes asymmetric.

We can independently control the peak position and peak width by tuning two ring resonators. In Fig. 2(b), we show that we can maintain the width of the transparency window while changing the position by red-shifting or blue-shifting the two rings together. We can also change the width and Q-factor of the transmission peak while fixing the position [Fig. 2(c)]. Bringing two ring resonators closer in terms of resonance wavelengths results in a narrower transparency window (higher Q-factor), and vice versa. The height of the transmission peak is a function of both detuning and loss [Eq. (4)]. Thus a high-Q transparency window may have lower overall transmission. Designing the device with lower-loss waveguides would mitigate this issue. Note that every scenario in Figs. 2(b) and 2(c) is on-resonance, so the phase shifters between two rings are tuned when we change the peak position.

For a filter design involving a single resonator, the resonance wavelength and Q-factor are usually dependent on each other, because the change of loss often accompanies the tuning process. In the BIC filter, however, the transparency window is not the mode of an individual resonator, but the mode of the near-BIC state. Therefore, the position and width of the transparency window are independent of each other. This flexibility is very desirable in PICs [29].

If one intends to use the BIC filter as an optical switch, there are three approaches. We regard the blue curve in Fig. 2(a) as the "on" state for 1533 nm wavelength; then we can turn the transmission off by any one of the following

approaches: (1) breaking the FP resonance [Fig. 3(a) yellow curve, 22 dB on-off ratio]; (2) shifting the peak position [Fig. 2(b) purple or green curve, 25 dB on-off ratio]; and (3) constructing exact-BIC state [Fig. 1(h), 75 dB on-off ratio]. Simulation reproduction of Figs. 2(a)–2(c) with high consistency can be found in Fig. 5.

Scalability is a great advantage of our platform. We can cascade more detuned resonators sharing the same buses so that the transmission spectrum will show a series of tunable peaks [24]. As a demonstration of this concept, we design a triple-resonator device with an additional ring ($r_3 = 15.02\,\mu m$) shown in Fig. 3(a). The two loops between two adjacent rings give rise to two transparency windows when the system is on-resonance.

In Fig. 3(b), we show the effect when we fix the resonance wavelengths of three rings and the phase delay in the second loop while increasing the phase delay in the first loop. The second peak is fixed in place, but the first peak red-shifts until it merges into the right-hand peak. It promises the possibility of having two transparency windows (blue curve) or eliminating either one of them (yellow curve). Figure 3(c) is the simulation result of the same process, confirming the effect of tuning phase delay in one of the loops.

Because of the thermal cross talk in the fabricated device, we use simulations to demonstrate the potential of individual peak tuning in Fig. 3(d). Starting from two peaks with similar widths (blue curve), we can control the resonances of three rings so that the center frequency in the first loop is constant while the detuning in the second loop remains fixed. The result is that the left-hand peak
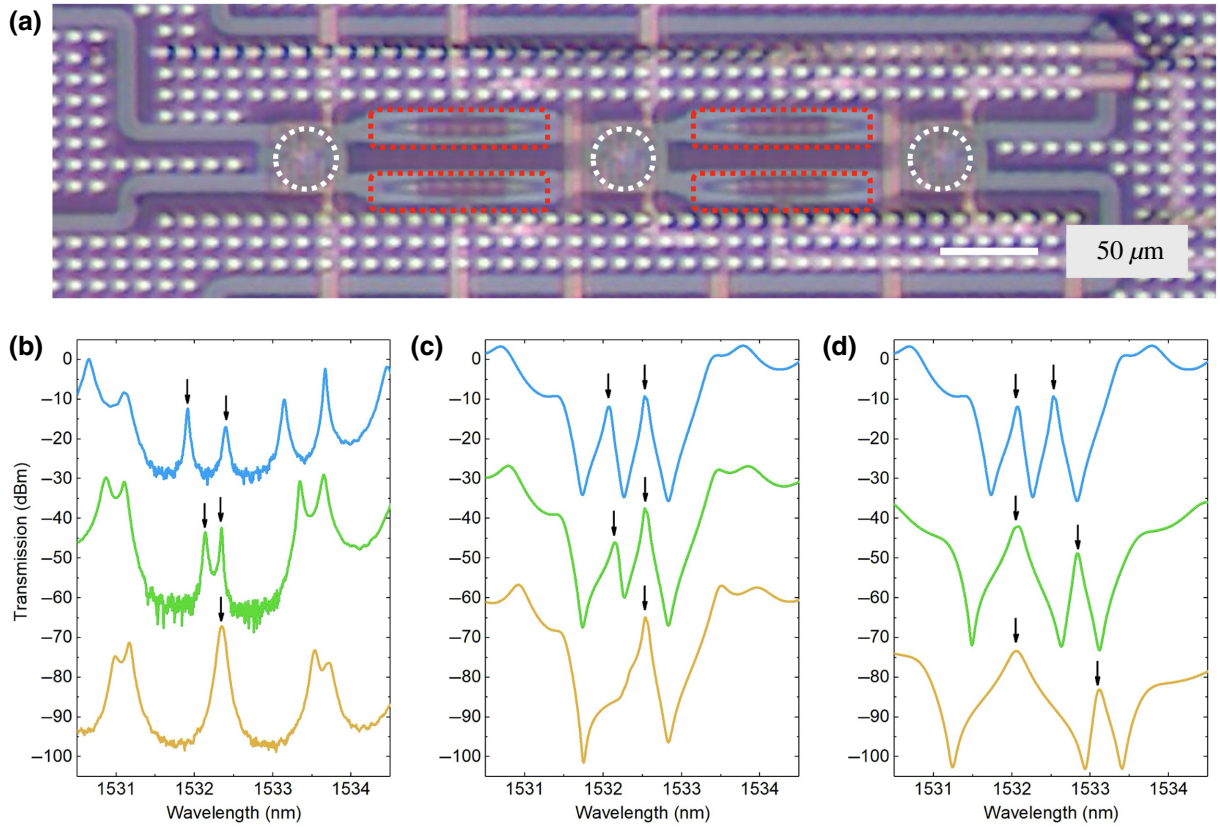
FIG. 3. (a) Optical image of the triple-resonator device. White circles denote the ring resonators, red rectangles are the thermo-optic phase shifters. The left-hand and middle rings are the first loop, the middle and right-hand rings are the second loop. (b) Tuning the phase delay in the first loop. The blue curve is the on-resonance case for both loops with two transmission peaks. (c) Simulation reproduction of (b). (d) Tuning the right-hand peak's position with fixed width while tuning the left-hand peak's width (Q-factor) with fixed position. Spectra in (d) are all on-resonance in both loops. Blue curves in (c) and (d) are the same. Black arrows are used as a guide to the peaks of interest in each panel. All the curves are shifted vertically for clear illustration.

has a fixed position but varying width, while the right-hand peak has a fixed width at different positions. The Q-factor of the left-hand peak changes from 1.82×10^4 in the blue curve to 9.05×10^3 and 6.65×10^3 in the green and yellow curves, respectively. The position of the right-hand peak shifts by 4 times and 7.66 times the full width at half maximum in the green and yellow curves, respectively, compared to the blue curve. Note that every scenario here is on-resonance for both loops. This phenomenon follows the same principle as the dual-resonator device and further proves the versatility of the BIC filters.

To realize the full potential of the cascaded ring resonator system, the following device optimizations are desirable: (1) an optical system with lower loss using a ridge waveguide (larger resonator rings may also help) and (2) carrier-injection modulation that avoids thermal cross talk and achieves higher modulation speed.

In conclusion, we demonstrate dynamically tunable near-BIC states using a PIC platform, which are highly promising for multiple on-chip functionalities. The cascaded resonators bring about the near-BIC state, which

has high transmission and is used to construct a transparency window. We argue that this phenomenon fits the BIC formalism rather than the rigorous optical analog of EIT. Furthermore, the devices we demonstrate are versatile filters whose peak position and width can be independently controlled. They can also be used as optical switches. We believe the results could deepen our understandings of the general BIC concept and help lower the threshold for its applications.

APPENDIX A: TRANSMISSION CHARACTERISTICS FOR THE RESONATOR SYSTEM USING TEMPORAL-COUPLED-MODE THEORY

The two cascaded resonators have their intrinsic resonance frequencies ω_1 and ω_2, respectively. $\omega_o = (\omega_1 + \omega_2)/2$ is the center frequency and $\Delta = (\omega_1 - \omega_2)/2$ is the resonance detuning. The probe beam's frequency is ω, and the detuning frequencies between the probe beam and the two resonators are $\Delta_{1(2)} = \omega - \omega_{1(2)}$, respectively. The intrinsic decay rate is $\gamma_i/2$ for both resonators; the coupling rate is $\gamma_c/2$ at all the gaps. Following the electric field amplitude denoted in the schematic representation [Fig. 1(a)], we can describe the amplitude relations at steady state using a system of equations [18]:

$$
\begin{cases}
\left[i\Delta_1 - \left(\frac{\gamma_i}{2} + \gamma_c\right)\right]a_1 - \sqrt{\gamma_c}A_1 - \sqrt{\gamma_c}A_6 = 0, \\
\left[i\Delta_2 - \left(\frac{\gamma_i}{2} + \gamma_c\right)\right]a_2 - \sqrt{\gamma_c}A_3 = 0, \\
A_3 = A_2 = A_1 + \sqrt{\gamma_c}a_1, \\
A_6 = A_7 = \sqrt{\gamma_c}a_2, \\
A_4 = A_3 + \sqrt{\gamma_c}a_2.
\end{cases}
\tag{A1}
$$
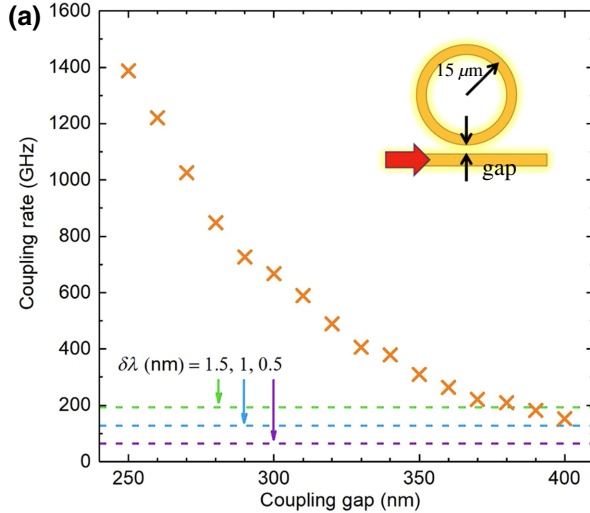
The transmission is

$$
T = \left|\frac{A_4}{A_1}\right|^2 = t^2,
\tag{A2}
$$

$$
t = \frac{-\Delta_1\Delta_2 - i(\gamma_i/2)(\Delta_1 + \Delta_2) + (\gamma_i^2/4)}{-\Delta_1\Delta_2 - i[\gamma_c + (\gamma_i/2)](\Delta_1 + \Delta_2) + \gamma_c\gamma_i + (\gamma_i^2/4)}.
\tag{A3}
$$

If we assume $\gamma_c \gg \Delta \gg \gamma_i \to 0$, at $\omega = \omega_o$ and $\Delta_1 = \Delta_2 = \Delta$:

$$
t_{\text{BIC}} = \frac{\Delta^2 + (\gamma_i^2/4)}{\Delta^2 + \gamma_c\gamma_i + (\gamma_i^2/4)} \approx \frac{\Delta^2}{\Delta^2 + \gamma_c\gamma_i} \to 1.
\tag{A4}
$$

If the probe frequency coincides with one of the intrinsic resonance frequencies of the two resonators:

$$
t_{\omega_1(\omega_2)} = \frac{\pm i\gamma_i\Delta + (\gamma_i^2/4)}{\pm i\gamma_i\Delta \pm 2i\gamma_c\Delta + \gamma_c\gamma_i + (\gamma_i^2/4)}
$$
$$
\approx \frac{1}{1 + 2(\gamma_c/\gamma_i) \mp i(\gamma_c/\Delta)} \to 0.
\tag{A5}
$$

From the discussions above, we conclude the essential requirements for a versatile BIC filter: first, the intrinsic loss needs to be small, otherwise the height of the transmission peak decreases; second, the coupling rate between the resonator and the bus should be high enough to ensure $\gamma_c \gg \Delta$; third, we need to fine-tune the intrinsic resonance frequencies and the phase delay between the resonators.
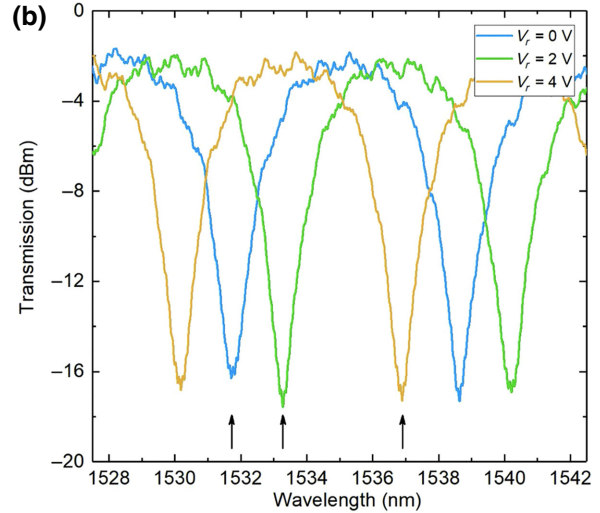

FIG. 4. (a) Simulation of the single-bus coupling rate ($\gamma_c/2$) as a function of gap size using a 15-μm-radius ring and a single bus waveguide (width of 300 nm and resonant wavelength of 1533 nm). Dashed lines indicate frequency detunings from the resonant wavelength. (b) Measured transmission spectra of a single 15-μm-radius ring resonator with double-bus coupling. V_r is the voltage of the thermo-optic heater near the ring resonator. The black arrow shows the same transmission dip under different ring heater voltages.

APPENDIX B: BIC FILTER DEVICE DESIGN

We design the proposed device using a silicon photonics platform with 220-nm silicon-on-insulator wafers [Fig. 1(b)]. The two ring resonators have slightly different radii ($r_1 = 14.98\,\mu$m; $r_2 = 15\,\mu$m), and they are controlled by thermo-optic heaters (controlled by voltages V_1 and V_2). Thermo-optic phase shifters connect the two ring resonators, and they are controlled by voltage V_t. The bus waveguides and resonator waveguides all have a base width of 300 nm. All the coupling gaps (g) between bus waveguides and ring resonators are 300 nm to enforce identical coupling rates ($\gamma_c/2$). AIM Photonics Foundry fabricated the device through a multiproject wafer run [30]. The simulations are carried out in Lumerical MODE and INTERCONNECT [31].

We simulate the coupling rate between a 15-μm ring and a single bus waveguide in Fig. 4(a) as a function of gap size (g) at a resonance wavelength of 1533 nm. The cross section of all waveguides is 220 nm in height and 300 nm

in width. The background material is silica. The coupling rate increases exponentially as the gap size decreases. The three dashed lines are examples of frequency detunings from the resonance. Note that the devices in the discussions typically have $\delta\lambda < 1$ nm. Comparing the orange data points with the dashed lines, we can conclude that $\gamma_c/2 \gg \Delta$ at $g = 300$ nm. This complies with the criterion that brings about significant transmission peak. In Fig. 4(b), we show the ring heater's capability for tuning a single-ring device ($r = 15\,\mu$m) over most of the free spectral range. It lays a solid foundation for device demonstrations.

Figure 5 shows the simulation results of the filter device, depicting the BIC-protected transmission peak and the tunability. To match the fabricated device, the cross section of all waveguides is 220 nm in height and 300 nm in width. The coupling gap is 300 nm at all coupling ports. The background material is silica. The radii of the first and second rings are 14.98 and 15.00 μm, respectively. We tune the refractive indices of the two rings separately to simulate V_1 and V_2. We also tune the length of the bus waveguide
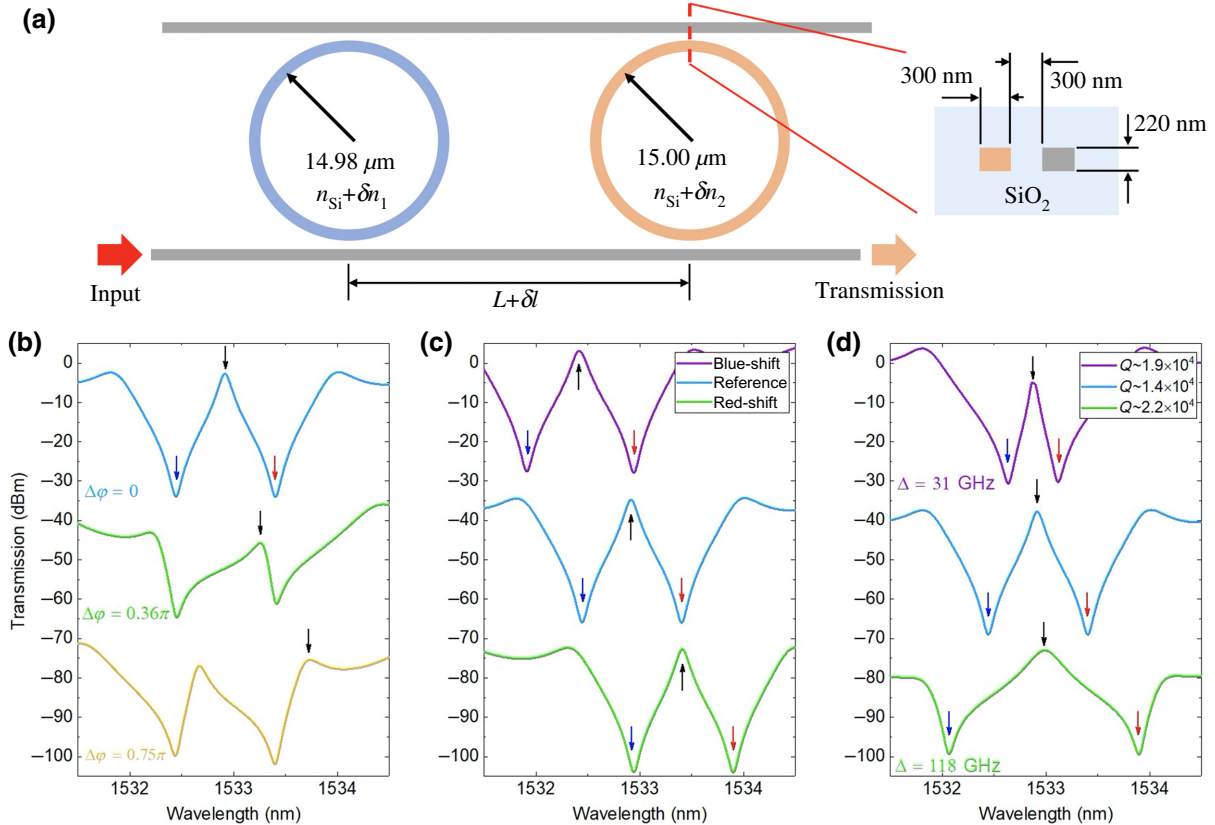

FIG. 5. (a) Schematic of the simulation structure. (b)–(d) Simulation reproduction of Fig. 2. Unless noted beside the curves, the default parameters to the BIC model are: $\Delta = 61$ GHz; $\gamma_c/2 = 667$ GHz; $\Delta\varphi = 0$. All the curves are shifted vertically for clear illustration. Black, blue, and red arrows highlight ω_o, ω_1, and ω_2, respectively, as described in Eqs. (4) and (5). The simulation results reproduce the experimental data. The simulations show apparent transmission dips indicating intrinsic resonance wavelengths of the rings. Note that the curvature near the peak is slightly different in the simulations compared with the experiments, which also results in larger Q-factors for the windows. This is due to the additional loss in the fabricated device that causes the transmission to fall off quickly around near-BIC points.

between the rings to simulate V_t. The simulation agrees with the experimental results very well (Fig. 2).

[1] C. W. Hsu, B. Zhen, A. D. Stone, J. D. Joannopoulos, and M. Soljac, Bound states in the continuum, Nat. Rev. Mater. **1**, 16048 (2016).

[2] J. D. Joannopoulos, S. G. Johnson, J. N. Winn, and R. D. Meade, *Molding the Flow of Light* (Princeton University Press, Princeton, NJ, 2008).

[3] K. Sakoda, Optical properties of photonic crystals, Springer Sci. Bus. Media **80**, 43 (2004).

[4] C. W. Hsu, B. Zhen, J. Lee, S. L. Chua, S. G. Johnson, J. D. Joannopoulos, and M. Soljačić, Observation of trapped light within the radiation continuum, Nature **499**, 188 (2013).

[5] B. Zhen, C. W. Hsu, L. Lu, A. D. Stone, and M. Soljačić, Topological Nature of Optical Bound States in the Continuum, Phys. Rev. Lett. **113**, 257401 (2014).

[6] L. Lu, J. D. Joannopoulos, and M. Soljačić, Topological photonics, Nat. Photonics **8**, 821 (2014).

[7] E. N. Bulgakov and A. F. Sadreev, Robust bound state in the continuum in a nonlinear microcavity embedded in a photonic crystal waveguide, Opt. Lett. **39**, 5212 (2014).

[8] A. Kodigala, T. Lepetit, Q. Gu, B. Bahari, Y. Fainman, and B. Kanté, Lasing action from photonic bound states in continuum, Nature **541**, 196 (2017).

[9] S. T. Ha, Y. H. Fu, N. K. Emani, Z. Pan, R. M. Bakker, R. Paniagua-Domínguez, and A. I. Kuznetsov, Directional lasing in resonant semiconductor nanoantenna arrays, Nat. Nanotechnol. **13**, 1042 (2018).

[10] J. Jin, X. Yin, L. Ni, M. Soljačić, B. Zhen, and C. Peng, Topologically enabled ultrahigh-Q guided resonances robust to out-of-plane scattering, Nature **574**, 501 (2019).

[11] Y. Zhang, A. Chen, W. Liu, C. W. Hsu, B. Wang, F. Guan, X. Liu, L. Shi, L. Lu, and J. Zi, Observation of Polarization Vortices in Momentum Space, Phys. Rev. Lett. **120**, 186103 (2018).

[12] H. M. Doeleman, F. Monticone, W. Den Hollander, A. Alù, and A. F. Koenderink, Experimental observation of a polarization vortex at an optical bound state in the continuum, Nat. Photonics **12**, 397 (2018).

[13] J. Lee, B. Zhen, S. L. Chua, W. Qiu, J. D. Joannopoulos, M. Soljačić, and O. Shapira, Observation and Differentiation of Unique High-Q Optical Resonances Near Zero Wave Vector in Macroscopic Photonic Crystal Slabs, Phys. Rev. Lett. **109**, 067401 (2012).

[14] J. Gomis-Bresco, D. Artigas, and L. Torner, Anisotropy-induced photonic bound states in the continuum, Nat. Photonics **11**, 232 (2017).

[15] Z. Yu, Y. Tong, H. K. Tsang, and X. Sun, High-dimensional communication on etchless lithium niobate platform with photonic bound states in the continuum, Nat. Commun. **11**, 2602 (2020).

[16] W. Bogaerts, R. Baets, P. Dumon, V. Wiaux, S. Beckx, D. Taillaert, B. Luyssaert, J. Van Campenhout, P. Bienstman, and D. Van Thourhout, Nanophotonic waveguides in silicon-on-insulator fabricated with CMOS technology, J. Light. Technol. **23**, 401 (2005).

[17] Z. Wang, S. Fan, and W. Suh, Temporal coupled-mode theory and the presence of non-orthogonal modes in lossless multimode cavities, IEEE J. Quantum Electron. **40**, 1511 (2004).

[18] Q. Li, T. Wang, Y. Su, M. Yan, and M. Qiu, Coupled mode theory analysis of mode-splitting in coupled cavity system, Opt. Express **18**, 8367 (2010).

[19] S. Fan and W. Suh, Temporal coupled-mode theory for the fano resonance in optical resonators, J. Opt. Soc. Am. A **20**, 569 (2003).

[20] Y. C. Liu, B. B. Li, and Y. F. Xiao, Electromagnetically induced transparency in optical microcavities, Nanophotonics **6**, 789 (2017).

[21] S. Manipatruni, P. Dong, Q. Xu, and M. Lipson, Tunable superluminal propagation on a silicon chip, Opt. Lett. **33**, 2928 (2008).

[22] J. Pan, Y. Huo, S. Sandhu, N. Stuhrmann, M. L. Povinelli, J. S. Harris, M. M. Fejer, and S. Fan, Tuning the coherent interaction in an on-chip photonic-crystal waveguide-resonator system, Appl. Phys. Lett. **97**, 101102 (2010).

[23] L. Zhou, T. Ye, and J. Chen, Coherent interference induced transparency in self-coupled optical waveguide-based resonators, Opt. Lett. **36**, 13 (2011).

[24] Y. F. Xiao, X. B. Zou, W. Jiang, Y. L. Chen, and G. C. Guo, Analog to multiple electromagnetically induced transparency in all-optical drop-filter systems, Phys. Rev. A - At. Mol. Opt. Phys. **75**, 063833 (2007).

[25] Q. Xu, S. Sandhu, M. L. Povinelli, J. Shakya, S. Fan, and M. Lipson, Experimental Realization of an on-Chip all-Optical Analogue to Electromagnetically Induced Transparency, Phys. Rev. Lett. **96**, 123901 (2006).

[26] M. Mancinelli, P. Bettotti, J. M. Fedeli, and L. Pavesi, Reconfigurable optical routers based on coupled resonator induced transparency resonances, Opt. Express **20**, 23856 (2012).

[27] B. Peng, ŞK Özdemir, W. Chen, F. Nori, and L. Yang, What is and what is not electromagnetically induced transparency in whispering-gallery microcavities, Nat. Commun. **5**, 5082 (2014).

[28] C. Wang, X. Jiang, G. Zhao, M. Zhang, and C. Wei, Electromagnetically induced transparency at a chiral exceptional point, Nat. Phys. **16**, 334 (2020).

[29] L. Chen, N. Sherwood-Droz, and M. Lipson, Compact bandwidth tunable microring resonators, Opt. InfoBase Conf. Pap. 32, 3361 (2008).

[30] E. Timurdogan, Z. Su, C. V. Poulton, M. J. Byrd, S. Xin, R. J. Shiue, B. R. Moss, E. S. Hosseini, and M. R. Watts, in *2018 Opt. Fiber Commun. Conf. Expo. OFC 2018 - Proc.* 1 (2018).

[31] Lumerical Inc., https://www.lumerical.com/products/.